The pristine interior of comet 67P revealed by the combined Aswan outburst and cliff collapse

M. Pajola[*,1,2], S. Höfner[3], J.B. Vincent[3,4], N. Oklay[3,4], F. Scholten[4], F. Preusker[4], S. Mottola[4], G. Naletto[2,5,6], S. Fornasier[7], S. Lowry[8], C. Feller[7], P.H. Hasselmann[7], C. Güttler[3], C. Tubiana[3], H. Sierks[3], C. Barbieri[2,9], P. Lamy[10], R. Rodrigo[11,12], D. Koschny[13], H. Rickman[14,15], H.U. Keller[4,16], J. Agarwal[3], M.F. A'Hearn[17], M.A. Barucci[7], J.-L. Bertaux[18], I. Bertini[2], S. Besse[19], S. Boudreault[3], G. Cremonese[20], V. Da Deppo[6], B. Davidsson[21], S. Debei[22], M. De Cecco[23], J. Deller[3], J.D.P. Deshapriya[7], M.R. El-Maarry[24,25], S. Ferrari[2], F. Ferri[2], M. Fulle[26], O. Groussin[10], P. Gutierrez[27], M. Hofmann[3], S.F. Hviid[4], W.-H. Ip[28,29], L. Jorda[10], J. Knollenberg[4], G. Kovacs[3,30], J.R. Kramm[3], E. Kührt[4], M. Küppers[19], L.M. Lara[27], Z.-Y. Lin[28], M. Lazzarin[9], A. Lucchetti[20], J.J. Lopez Moreno[27], F. Marzari[9], M. Massironi[31], H. Michalik[32], L. Penasa[31], A. Pommerol[24], E. Simioni[6,20], N. Thomas[24], I. Toth[33,10], E. Baratti[34].

* M. Pajola (corresponding author). Email: maurizio.pajola@nasa.gov; maurizio.pajola@gmail.com
1 NASA Ames Research Center, Moffett Field, CA 94035, USA.
2 Center of Studies and Activities for Space, CISAS, "G. Colombo", University of Padova, via Venezia 15, 35131 Padova, Italy.
3 Max-Planck-Institut für Sonnensystemforschung, Justus-von- Liebig-Weg, 3 37077 Göttingen, Germany.
4 Deutsches Zentrum für Luft- und Raumfahrt (DLR), Institut für Planetenforschung, Rutherfordstrasse 2, 12489 Berlin, Germany.
5 Department of Information Engineering, University of Padova, via Gradenigo 6/B, 35131 Padova, Italy.
6 CNR-IFN UOS Padova LUXOR, via Trasea 7, 35131 Padova, Italy.
7 LESIA, Observatoire de Paris, PSL Research University, CNRS, Univ. Paris Diderot, Sorbonne Paris Cité, UPMC Univ., Paris 06, Sorbonne Universités, 5 Place J. Janssen, Meudon Principal Cedex 92195, France.
8 The University of Kent, School of Physical Sciences, Canterbury, Kent CT2 7NZ, UK.
9 Department of Physics and Astronomy "G. Galilei", University of Padova, Vic. Osservatorio 3, 35122 Padova, Italy.
10 Aix-Marseille Université, CNRS LAM (Laboratoire d'Astrophysique de Marseille), UMR 7326, 13388 Marseille, France.
11 Centro de Astrobiologia, CSIC-INTA, 28850 Torrejon de Ardoz, Madrid, Spain.
12 International Space Science Institute, Hallerstrasse 6, 3012 Bern, Switzerland.
13 Scientific Support Office, European Space Research and Technology Centre/ESA, Keplerlaan 1, Postbus 299, 2201 AZ Noordwijk ZH, The Netherlands.
14 Department of Physics and Astronomy, Uppsala University, 75120 Uppsala, Sweden.
15 PAS Space Reserch Center, Bartycka 18A, 00716 Warszawa, Poland.
16 Institut für Geophysik und extraterrestrische Physik (IGEP), Technische Universität Braunschweig, Mendelssohnstr. 3, 38106 Braunschweig, Germany.
17 Department for Astronomy, University of Maryland, College Park, MD 20742-2421, USA.
18 LATMOS, CNRS/UVSQ/IPSL, 11 boulevard d'Alembert, 78280 Guyancourt, France.
19 Operations Department European Space Astronomy Centre/ESA, P.O. Box 78, 28691 Villanueva de la Canada, Madrid, Spain.
20 INAF Osservatorio Astronomico di Padova, Vic. Osservatorio 5, 35122 Padova, Italy.
21 NASA Jet Propulsion Laboratory, 4800 Oak Grove Drive, Pasadena, CA 91109, USA.
22 Department of Mechanical Engineering, University of Padova, via Venezia 1, 35131 Padova, Italy.
23 UNITN, University of Trento, via Mesiano, 77, 38100 Trento, Italy.
24 Physikalisches Institut der Universität Bern, Sidlerstr. 5, 3012 Bern, Switzerland.
25 Laboratory for Atmospheric and Space Physics, University of Colorado, 3665 Discovery Drive, CO 80301, USA.
26 INAF Osservatorio Astronomico di Trieste, via Tiepolo 11, 34143 Trieste, Italy.
27 Instituto de Astrofisica de Andalucia CSIC, Glorieta de la Astronomia, 18008 Granada, Spain.
28 Institute for Space Science, National Central University, 32054 Chung-Li, Taiwan.
29 Space Science Institute, Macau University of Science and Technology, Macau, China.
30 Budapest University of Technology and Economics, Budapest, Hungary.
31 Geosciences Department, University of Padova, via G. Gradenigo 6, 35131 Padova, Italy.
32 Institut für Datentechnik und Kommunikationsnetze der TU Braunschweig, Hans-Sommer-Str. 66, 38106 Braunschweig, Germany.
33 Observatory of the Hungarian Academy of Sciences, PO Box 67, 1525 Budapest, Hungary.
34 School of Civil Engineering, Department DICAM, University of Bologna, Bologna, Italy.

Introduction Paragraph

Outbursts occur commonly on comets [1], with different frequencies and scales [2,3]. Despite multiple observations suggesting various triggering processes [4,5], the driving mechanism is still poorly understood. Landslides have been invoked to explain some outbursts on comet 103P/Hartley 2 [6], although the process required a pre-existing dust layer on the verge of failure. The Rosetta mission observed several outbursts from its target comet 67P/Churyumov-Gerasimenko, which were attributed to dust generated by crumbling of materials from collapsing cliffs [7,8]. However, none of the aforementioned works included definitive evidence that landslides occur on comets. Amongst the many features observed by Rosetta on the nucleus of the comet, one peculiar fracture 70 m long and 1 m wide was identified on images obtained in September 2014 at the edge of a cliff named Aswan [9]. On 10 July 2015 the Rosetta Navigation Camera captured a large plume of dust that could be traced back to an area encompassing the Aswan escarpment [7]. Five days later, the OSIRIS camera observed a fresh, sharp and bright edge on the Aswan cliff. Here we report the first unambiguous link between an outburst and a cliff collapse on a comet. We establish a new dust-plume formation mechanism that does not necessarily require the breakup of pressurised crust or the presence of super volatile material, as suggested by previous studies [7]. Moreover, the collapse revealed the fresh icy interior of the comet, which is characterised by an albedo > 0.4, and provided the opportunity to study how the crumbling wall settled down forming a new talus.

Main text

The evolution of the collapse of the Aswan cliff [9], observed by the OSIRIS Narrow Angle Camera (NAC, [10]) and the Rosetta Navigation camera (NavCam) is shown in Fig. 1. We estimated a total outburst ejected mass of cometary material between $0.5\text{-}1.0\times10^6$ kg for the 10 July event. By applying stereo-photogrammetric methods (SPG, [11]) using multiple OSIRIS images (Supplementary Table 1), we determined the total volume of material that collapsed from the Aswan cliff. In Fig. 2, the dataset that depicts the aspect of the cliff before and after the collapse is presented. By using pre- and post-collapse 3D models (see Methods) we have been able to measure the dimensions of the collapsed overhang (Supplementary Figures 1-2), deriving a total volume of 2.20×10^4 m³, with a 1σ uncertainty of 0.34×10^4 m³.

On 19 July 2015, the interior of 67P's Aswan cliff was imaged with all NAC filters (Supplementary Table 1), facilitating the spectrophotometric study of five areas located on the wall (see Fig. 3 A, B and Methods). This analysis showed that the edge of the cliff (the green triangle in Fig. 3 B, C and D) was found to be highly saturated in the 600-900 nm range (the image acquired on 15 July 2015 (Fig. 1C) at 649.2 nm was saturated as well). As a result, the normal albedo of this area is only a lower limit, resulting in values > 0.40 at 650 nm, i.e. at least 6 times brighter than the overall surface of the nucleus itself [12]. High albedo regions on the 67P nucleus have been associated with the exposure of water ice observed in clustered bright spots in both hemispheres [13-15]. For these reasons, the spectrophotometric behaviour of the Aswan cliff indicates a clear exposure of pristine material enriched in water ice. On the contrary, the Aswan plateau shows a steeper and redder trend similar to other dark, dusty deposits of 67P [12]. The presence of fresh exposed water ice on the cliff face is indirectly confirmed by the temporal evolution of its normal albedo. On 26 December 2015 the bright cliff was imaged again with the NAC (Fig. 1D), and the resulting normal albedo at its edge was 0.16-0.18 (50% less than ~ 5 months before, i.e. most of the exposed water ice had already sublimated). On 6 August 2016, we re-computed the normal albedo on data with a higher spatial resolution (Supplementary Table 1), and determined that the cliff has returned to the dark value (< 0.12 at 650 nm) similar to the 67P terrains depleted in volatiles [12] (Fig. 3 G, Methods).

Despite that, there is still one bright block (ROI#1 Fig. 3 G,H,I) visible on the wall characterised by a normal albedo ~ 0.18: this is the biggest remnant of the originally exposed water ice.

Laboratory experiments [16] showed that diurnal thermal cycles lead to thermal stresses that can breakdown consolidated material into smaller pieces to form the fine regolith that is observed on asteroid surfaces, as well as contributing to rock breakdown on Earth [17,18]. Recent studies based on OSIRIS images have speculated that thermal stresses may influence surface features on 67P as well [19], eventually predisposing cliffs collapses [20]. In addition, [21] indicated that abrupt diurnal temperature changes in 67P's neck region occur due to mutual shadowing effects between the two lobes, suggesting that the early activity of the comet was correlated with temperature-related effects causing thermal cracking that propagates into the interior and induces sublimation within the crack itself [22,23]. In order to investigate whether thermal effects (or thermal cracking) could be the predisposing factors that weakened the already fractured Aswan cliff structure, we have carried out an analysis of the thermophysical conditions at the cliff before its breakdown (Fig. 4, Methods). We chose two facets that represent the diverging conditions occurring on the cliff (Fig. 4A). The cliff wall facet is located at the bottom of the sheet that created the landslide, i.e. where thermal cracking might be more important. Contrarily, the plateau facet shows the thermal environment on top of the cliff, at the location of the opening fracture. 67P's equinox was passed on 10 May 2015, and less than 2 months later the sub-solar point had already moved to 30° south. The north-facing neck areas of 67P drastically changed their illumination pattern, and instead of being illuminated twice per day, their periods of direct illumination became much shorter. In contrast, the Aswan cliff face was directly and perpendicularly illuminated for just ~1.5 h (Supplementary Video 1). This situation led to high maximum heat flux values of up to 740 W/m^2 on 10 July 2015, against the 450 W/m² at equinox. In contrast, the fractured plateau situated above the cliff did not receive direct sunlight except for short periods (maximum 66 W/m²) in July, versus the 270 W/m² of May 2015 (Fig. 4B). Despite shorter illumination durations and a smaller heliocentric distance in July, our thermal simulations show more extreme temperatures than those at equinox. Calculated surface temperatures vary between 100 and 340K at the cliff wall and between 85 and 180K at the plateau (Fig. 4C and D), whereas in May the simulated temperatures vary between 130-315K and 105-260K respectively (the temperature range decreases when we consider deeper layers – at a depth of 0.01 m both simulations show a range of 50 K or less (Fig. 4C and D).). The reason for this behaviour is the bilobate shape of 67P and the tilt of its rotation axis [24,25], which leads to nearly perpendicular illumination conditions on the cliff at local sunrise in July. Supported by the low thermal inertia of the surficial layers of 67P (15-50 $J\,m^{-2}s^{-1/2}K^{-1}$, [26,27]), a strong temperature rise of the upper layers occurs. At the cliff, the surface temperature rises from 130 to 320K in ~20 minutes (Supplementary Figure 3A, B), with a maximum of 30K/min shortly after sunrise. Subsurface layers (e.g. at 1 mm depth) still exhibit significant temperature rates-of-change up to 12 K/min. The low thermal conductivity induces high temperature gradients in the upper layers of the cliff face, with a maximum of 155 K/mm and exceeding 40 K/mm for about an hour (Fig. 4E), although these numbers depend on the detailed thermal properties of the surface layer. The plateau shows significantly lower gradients, 95 K/mm for May and 55 K/mm in July (Fig. 4F). Remarkably, deeper cometary layers still exhibit gradients in the order of 10 K/mm, being maintained for about an hour. While the integrated diurnal insolation on the Aswan cliff did not considerably increase in the months before the collapse, the cliff temperatures drastically changed. In the same timescale, the fractured plateau received less sunlight and cooled down significantly in the uppermost layers, but due to low thermal inertia of the material, temperature waves are not expected to penetrate to depths of more than a metre.

Despite such extreme factors, the collapse occurred during local midnight (denoted with the blue bars in Fig. 4). At this time, the thermal gradients have significantly lowered and became negative for all investigated depths. For this reason, it is not possible to suggest that such gradients have

eventually been the immediate triggering factor that led to the cliff collapse. Nevertheless, we underline that pervasive fracturing is present over the entire Aswan wall (both in the pre- and post-collapse case, Supplementary Figure 2). We therefore advance the idea that the diurnal thermal gradients, as well as their seasonal and annual variations, may have driven cyclic and cumulative opening of such fractures, in a process similar to that observed on Earth [17]. If thermal gradients have widened and deepened the fractures into the subsurface volatile-rich strata (as suggested in [22]), heat may have been transferred to deeper layers causing the loss of in-depth ice. Moreover, the gas suddenly released by the subliming material could have been infiltrated within the fractures [23] broadening them as well. For this reason, we suggest that the cumulative effect lead by the thermal gradients could be a weakening factor of the cliff structure predisposing it to the subsequent collapse (material anisotropy, voids and volatile sublimation can be others).

The Aswan cliff collapse is the first one witnessed on the surface of a cometary nucleus. To complement the above results and to provide a complete picture of the effects of this event, we focused on the newly-appeared deposit located at the cliff feet. Using three NAC images (Supplementary Table 1), we identified all boulders $\geq$ 1.5 m in size located on the Aswan talus, before and after the collapse (Fig. 5, Methods). The resulting pre-collapse cumulative number of boulders $\geq$ 1.5 m is 11784/km^2, while after the breakdown, this number changed to 18438/km^2. Such increase of density and surface roughness is evident in Fig. 5 and is not biased by a different spatial scale of the images (Supplementary Table 1). On the contrary, this is due to the increase of the boulder sizes in the 1.5-3.0 m range, as a result of the collapse itself. Indeed, the boulders' size-frequency distribution (SFD, Methods and Supplementary Material) indicates that the crumbling wall has produced predominantly smaller chunks. This is similarly observed on Earth, where the intrinsic weakness of the cliff material by penetrative fracturing strongly affects the resulting size of the debris, and typically results in a crumble of finer material, instead of only few large chunks [29]. Moreover, by extrapolating the SFD to smaller sizes (0.50 m), we estimate that 99% of the volume of the collapsed wall is distributed in the talus, in blocks ranging from 0.5 to 10 m in diameter. This means that 1% of this volume has been lost to space during the collapse. By assuming a density of 535 kg m^{-3} for the cometary material [11], this volume translates into 1.08×10^5 kg of material, consistent with our estimate of the mass present in the outburst plume.

On 67P, multiple taluses are identified in association with cliffs [20] suggesting that cliff collapses are important processes reshaping cometary surfaces. Eventually, thanks to the Rosetta OSIRIS and NavCam images we have witnessed such a breakdown, providing a definitive link between the collapse, the outburst event and the talus formation.

Main Text References

1) Hughes, D.W. Possible mechanisms for cometary outbursts, In: *R.L. Newburn Jnr., M. Neugebauer, J. Rahe (Eds.), Comets in the Post-Halley Era*, 2, Kluwer Academic Publishers, Dordrecht, pp. 825 (1999).

2) Lin, Z.Y. *et al.* The outburst of Comet 17P/Holmes. *Astron. Journal*, **138-2**, 625-632 (2009).

3) Farnham, T.L. *et al.* Dust coma morphology in the Deep Impact images of Comet 9P/Tempel 1. *Icarus* **187**, 26-40 (2007).

4) Tubiana, C., *et al.* 67P/Churyumov-Gerasimenko: Activity between March and June 2014 as observed from Rosetta/OSIRIS. *Astron. Astrophys.* **573**, A62, 11 pp. (2015).

5) Knollenberg, J. *et al.* A mini outburst from the nightside of comet 67P/Churyumov-Gerasimenko observed by the OSIRIS camera on Rosetta. *Astron. Astrophys.* **596**, A89, 10 pp. (2016).

6) Steckloff, J. K. *et al.* Rotationally induced surface slope-instabilities and the activation of CO2 activity on comet 103P/Hartley 2. *Icarus* **272**, 60-69 (2016).

7) Vincent, J. B. *et al.* Summer fireworks on comet 67P. *Mon. Not. R. Astron. Soc.* **462**, pp. S184-S194 (2016).

8) Grün, E. et al. The 2016 Feb 19 outburst of comet 67P/CG: an ESA Rosetta multi-instrument study. *Mon. Not. R. Astron. Soc.* **462**, pp. S220-S234 (2016).

9) Pajola, M. *et al.* Aswan site on comet 67P/Churyumov-Gerasimenko: Morphology, boulder evolution, and spectrophotometry. *Astron. Astrophys.* **592**, A69, 17 pp. (2016).

10) Keller, H. U. *et al.* OSIRIS—The scientific camera system onboard Rosetta. *Space Sci. Rev.* **128**, 433 (2007).

11) Preusker *et al.* Shape model, reference system definition, and cartographic mapping standards for comet 67P/Churyumov-Gerasimenko - Stereo-photogrammetric analysis of Rosetta/OSIRIS image data. *Astron. Astrophys.* **583**, A33, 19 pp (2015).

12) Fornasier, S. *et al.* Spectrophotometric properties of the nucleus of comet 67P/Churyumov-Gerasimenko from the OSIRIS instrument onboard the ROSETTA spacecraft. *Astron. Astrophys.* **583**, A30, 18 pp (2015).

13) Pommerol, A. *et al.* OSIRIS observations of meter-sized exposures of H_2O ice at the surface of 67P/Churyumov-Gerasimenko and interpretation using laboratory experiments. *Astron. Astrophys.* **583**, A25 (2015).

14) Barucci, M.A. *et al.* Detection of exposed H_2O ice on the nucleus of comet 67P/Churyumov-Gerasimenko, as observed by Rosetta OSIRIS and VIRTIS instruments. *Astron. Astrophys.* **595**, A102, 13 pp (2016).

15) Fornasier, S. *et al.* Rosetta's comet 67P/Churyumov-Gerasimenko sheds its dusty mantle to reveal its icy nature. *Science* **354**, 1566-1570 (2016).

16) Delbo, M. *et al.* Thermal fatigue as the origin of regolith on small asteroids. *Nature*, **508**, p. 233-236 (2014).

17) Collins, B. D and Stock, G. M. Rockfall triggering by cyclic thermal stressing of exfoliation fractures. *Nature Geosci.* **9**, 395-401 (2016).

18) Molaro, J. L., Byrne, S. and Langer, S. A. Grain-scale thermoelastic stresses and spatiotemporal temperature gradients on airless bodies, implications for rock breakdown. *J. Geophys. Res.* **120**, Issue 2, pp. 255-277 (2015).

19) El-Maarry, M. R. *et al.* Fractures on comet 67P/Churyumov-Gerasimenko observed by Rosetta/OSIRIS, *Geophys. Res. Lett.* **42**, 5170–5178 (2015).

20) Pajola, M. *et al.* Size-frequency distribution of boulders ≥7 m on comet 67P/Churyumov-Gerasimenko. *Astron. Astrophys.* **583**, A37, 17 pp (2015).

21) Ali-Lagoa, V. Delbo M., and Libourel G. Rapid Temperature Changes and the Early Activity on Comet 67P/Churyumov-Gerasimenko. *Astrophys. J. Lett.* **810**, article id. L22, 5 pp. (2015).

22) Vincent, J. B. *et al.* Are fractured cliffs the source of cometary dust jets? Insights from OSIRIS/Rosetta at 67P/Churyumov-Gerasimenko. *Astron. Astrophys.* **587**, A14, 15 pp (2015).

23) Skorov, Y.V. *et al.* A model of short-lived outbursts on the 67P from fractured terrains. *Astron. Astrophys.* **593**, A76, 10 pp (2016).

24) Sierks, H. *et al.* On the nucleus structure and activity of comet 67P/Churyumov-Gerasimenko. *Science* **347**, 1044 (2015).

25) Thomas, N. *et al.* The morphological diversity of comet 67P/Churyumov-Gerasimenko, *Science* **347**, Issue 6220, article id. aaa0440 (2015).

26) Schloerb, F. P. *et al.* MIRO observations of subsurface temperatures of the nucleus of 67P/Churyumov-Gerasimenko. *Astron. Astrophys.* **583**, A29, 11 pp (2015).

27) Gulkis, S. *et al.* Subsurface properties and early activity of comet 67P/Churyumov-Gerasimenko. *Science* **347**, 709 (2015).

28) Mottola, S. *et al.* The rotation state of 67P/Churyumov-Gerasimenko from approach observations with the OSIRIS cameras on Rosetta. *Astron. Astrophys.* **569**, id. L2, 5 pp (2015).

29) Mortimore R. N. and Duperret A. Coastal chalk cliff instability. *Geological Society of London* (2004).

Acknowledgements

Author Contributions

M.P. conceived, led and designed the study, analysed the cliff setting before and after the collapse, contributed to the spectrophotometric study, made the overall boulder size-frequency analysis and wrote the main text and Methods; S.H. carried out the thermophysical analysis and wrote part of the main text and Methods; J.B.V. performed the outburst analysis and wrote part of the main text; N.O.

carried out the 6 August 2016 post-collapse spectrophotometric analysis, wrote part of the main text and Methods; F.S. and F. P. were responsible for the stereo-photoclinometric model and the 3D reconstruction of the pre- and post-collapse cases, wrote part of the main text and Methods; S.M. contributed to the thermophysical analysis and made the illumination conditions video of 10 July 2015; G.N. contributed to designing the study and data interpretation; S.F carried out the 19 July 2015 spectrophotometric analysis, wrote part of the main text and Methods; S.L. contributed to the thermophysical analysis and wrote part of the main text; C.F. and P.H.H. contributed to the spectrophotometric study; C.G. and C.T. contributed to the data interpretation and made the Aswan observations possible; H.S., C.B., P.L., R.R., D.K. and H.R. are the lead scientists of the OSIRIS project. The other authors are all co-investigators who built and ran this instrument and made the observations possible, and associates and assistants who participated in the study.

Author Information

Correspondence and requests for materials should be addressed to M.P. (maurizio.pajola@gmail.com).

Main Figure Legends

Figure 1. **The Aswan cliff outburst. a,** OSIRIS NAC reference image taken on 4 July 2015. The Aswan cliff location on the main body of 67P is indicated with the red spot in the upper miniature (0). No bright features appear on the cliff yet. **b,** NavCam image taken on 10 July 2015. The white arrow shows the outburst occurred in the Aswan area. The usual, observed jet activity occurring over the illuminated side of the comet is also visible. **c,** OSIRIS NAC image obtained on 15 July 2015 showing the bright, pristine material on the cliff. **d,** OSIRIS NAC image taken on 12 December 2015, depicting the bright Aswan cliff.

Figure 2. **The Aswan cliff pre- and post-collapse.** NAC images taken at different spatial scales (0.1-0.5 m/pixel) showing the Aswan cliff and fracture setting before (**a,b,d** and **e**) and after (**c-f**) the collapse. The white circle shows the same boulder in all images. The white arrows show the fracture before the collapse and the new sharp edge after the collapse. The white box in **c** marks the location shown in Supplementary Figure 1.

Figure 3. **The spectrophotometric analysis after the cliff-collapse.** 19 July 2015 case includes **a-d** panels, while panels **e-i** are related to the 6 August 2016 case. **a,** RGB image obtained using the NAC images centred at 882 nm (R), 649 nm (G) and 480 nm (B). **b,** Zoom into the Aswan cliff and selection of the five regions of interest located along the cliff. **c,** Normal albedo computed for each area in each filter. The edge of the cliff represented by the green triangle is highly saturated, so the albedo is underestimated. **d,** Relative reflectance computed on the five regions of interest. **e** context NAC image. **f,** spectral slopes computed on the Aswan cliff. **g,** colour composite of the cliff using the images taken at 882.1 nm, 649.1 nm and 480.7 nm in the RGB channels respectively. Selected regions of interest (ROIs) are enumerated and overlaid. **h,** ROIs normal albedo. **i,** ROIs relative reflectance normalized at 480.7 nm.

Figure 4. **The thermophysical analysis on the Aswan cliff and plateau.** Thermophysical model results for 10-05-2015 and 10-07-2015 for 1.5 comet rotation of 12.4 hours [28]. In all panels the blue bar denotes the observed NavCam outburst cliff collapse time, while the red line indicates the rotation period. **a,** 3D view showing the location of the Aswan cliff wall and the plateau facets

where we derived the following plots. The temperatures are computed at 2.5 h of the simulation time (see Methods). **b,** Illumination conditions (heat flux by solar irradiation) on cliff wall and plateau on 10 July and 10 May 2015, respectively. These two dates are the same also for plots **c-e**. **c,** Temperatures for the cliff wall at three depths (surface, 5 and 10 mm). **d,** Temperatures for the plateau at three depths (surface, 5 mm and 10 mm). **e,** Average temperature gradients for the cliff wall at three depths (0-1mm, 0-5mm and 5-10mm). **f,** Average temperature gradients for the plateau at three depths (0-1mm, 0-5mm and 5-10mm).

Figure 5. **The talus boulder analysis during pre- and post-collapse.** First column: the three original NAC images used for the boulder identification. The white arrows show the illumination direction. Second column: the spatial distribution of the boulders grouped in size (m) present on three similar zoomed areas. The talus roughness and boulder density increase is observable in the post-breakdown images and is quantified in the Supplementary Material.

Methods

DTM Methodology and Anaglyph generation:

To compute the total volume that collapsed from the Aswan cliff, we applied stereo-photogrammetric methods (SPG [11]) using the highest resolution images available from the OSIRIS NAC camera. The specific location of the Aswan cliff on the comet's nucleus (close to the edge of the neck region between the two lobes and near 67P's north pole), as well as the illumination conditions during the Rosetta mission (typically high phase angles up to 90°) limit the number of OSIRIS NAC images suitable for stereo reconstruction. The most appropriate post-collapse stereo images in terms of geometric properties (high image resolution, sufficient stereo angles for reliable three-dimensional shape reconstruction), and in terms of proper illumination conditions (minimised cast shadowed areas) were taken during the SHAP8 OSIRIS NAC sequence on 8-9 June 2016. A set of three images (NAC_2016-06-08T14.34.26, NAC_2016-06-09T02.30.44, NAC_2016-06-09T14.43.35) provides views of the cliff with spatial scale of 0.5 m/pixel, combined with acceptable stereo and illumination conditions (10°-21° stereo angles, almost no cast shadows in the area of interest). We used this set within a SPG adjustment that relates the images to the sub-pixel accuracy level.

During the pre-collapse period, both illumination and viewing geometry were less favourable to stereo reconstruction. There is not a single set of images that display the cliff adequately for a reliable SPG reconstruction in high-resolution. Good illumination for the area of interest is available only for the images acquired during the early months of the Rosetta mission where the sub-solar latitude and incidence angles are high. Unfortunately, these images are characterised by a relatively low spatial scale (2-5 m/pixel). Nonetheless, later on in the mission, a few images provide much better spatial scale (up to ~1 m/pixel). Therefore, the overall SPG adjustment towards the global SHAP4S shape model [11] using all stereo-suitable OSIRIS NAC images provides the most complete and most accurate description of the Aswan cliff before its collapse, Supplementary Figure 1. The relevant subset of this global model and a model that we derived from SHAP8 images were finally used for the computation of the volume of the Aswan cliff that collapsed.

We first tied/aligned both 3D models together using surface features in the immediate vicinity of the collapse area as a reference and then computed the difference between both cliff volumes as 33.7×10^3 m^3, Supplementary Figure 1. It is obvious (from visual inspection of the pre-collapse images) that, as a result of particular deficits of the pre-collapse stereo dataset, the pre-collapse shape of the cliff is generally too flat and does not describe the cliff wall concavities well enough. We have taken this systematic effect into account and estimated the portion of unconsidered pre-

collapse concavity to 30-50%. Considering this effect, we get a final estimation of the overhanging volume of the collapsed Aswan cliff of 2.20×10^4 m³, with a 1-sigma uncertainty of 0.34×10^4 m³. In addition, four different anaglyphs of the Aswan area have been prepared in order to provide clear views that depict the cliff setting before and after the collapse, Supplementary Figure 2. In particular, by means of Supplementary Figure 2a and b, the overhanging nature (12 m at the block's top, 0 m at its feet) of the detaching block is evident.

Colour Analysis Methodology:

The normal albedo presented in Fig. 3c has been evaluated from images (Supplementary Table 1) that have been photometrically corrected using a Hapke model [30] and the parameters determined by [12, Table 4] from resolved photometry in the orange filter centred at 649.2 nm (filter called F22). We have assumed that the phase function at 649.2 nm also applies at the other wavelengths. Moreover the SHAP4S model was used to calculate the photometric angles at the time of the observation [11] to correct the images for different illumination conditions. The flux from the five regions of interest (ROI) in Fig. 3b,c,d in each of the 11 filters has been integrated over 2x2 pixel boxes, i.e. a surface of ~36 m^2.

The OSIRIS NAC images used in Fig. 3f,g,h,i (Supplementary Table 1) are sequentially recorded at 882.1 nm (F41), 649.2 nm (F22), 480.7 nm (F24). Therefore, they have to be co-aligned in order to eliminate colour artefacts created by misalignment of the images. The images are then photometrically corrected using the Lommel-Seeliger disk function [31] to eliminate the effects due to different illumination conditions. USGS ISIS3 [32] software is used for both corrections. The photometric angles are calculated from the 3D shape model described in [11], reduced to one million facets to limit the necessary computational time. The SPICE kernels are used with the 'SPICE toolkit for C' for the alignment of the shape at the observing time of the reference image (the one taken at 649.2nm). A detailed description of image registration and photometric correction of subsequent OSIRIS NAC images are described in [33], Appendix A.

The spectral slopes presented in Fig. 3f are calculated by using equation:

Spectral slopes (%/100nm)= [(F41-F24)×10000]/[F24×(882.1-480.7)]

This methodology is used to detect variegation within the region shown in Fig. 3e. The in-homogeneity of the exposed cliff and its vicinity is investigated in smaller regions (six different regions of interest (ROIs), four located on the wall (ROIs 1,2,3,4), and two on the overlying terrace; ROIs 5,6 of Fig. 3g), where some variegation was detected (see Main Text) via spectral slopes and RGB colours. The mean spectra within the selected regions are calculated (Fig. 3h). However, direct comparison between spectra is achieved by using spectra normalized at 480.7nm (Fig. 3i).

Thermophysical Analysis Methodology:

The goal of the thermophysical analysis is to work out the driving temperature conditions of the cliff between the time of its collapse, and the months before. We set up a thermophysical model that takes into account solar irradiation, shadowing, radiative heat exchange between cometary surfaces, and conductive heat transfer perpendicular to the uppermost layers of the cometary nucleus. For simplicity reasons, sublimation and phase-change effects are neglected, and we treat the cometary layers to have uniform thermophysical properties. We follow a widely used (e.g. [34-36]) 1D heat diffusion approach to determine temperatures and fluxes in the subsurface layers of the Aswan cliff:

$$\rho c \frac{\partial T}{\partial t} = \frac{\partial}{\partial x}\left(\lambda(T)\frac{\partial T}{\partial x}\right)$$

where ρ, c and $\lambda(T)$ describe material density, specific heat and thermal conductivity. The thermal conductivity of the cometary bulk material is assumed to be driven by radiative exchange and therefore temperature-dependant. We adopt an approach described in [37] (and references therein) that is based on the size of the agglomerates which constitute the cometary material. Hence, the obtained conductivity for agglomerates of 1mm size varies between 0.0005 W/mK and 0.02 W/mK in the temperature range between 100 and 370 K. The synthetic thermal inertia $\Gamma = \sqrt{\rho c \lambda}$ of the cometary material ranges between 15 and 90 $J\ m^{-2}s^{-1/2}K^{-1}$, which corresponds to the low inertia estimations, gained by measurements of 67Ps superficial layers by remote sensing, e.g. [38,39]. Such a low conductivity, which results in penetration depths of the thermal heat wave of a few centimeters negates the requirement for a 3D modelling approach.

The boundary condition at the surface node is described by

$$(1 - A)\frac{S}{AU^2}f_{illum}\cos\theta + F_{scatter} + \sum_j REF_{i,j}\ T_j^4 - \varepsilon\sigma T_i^4 - \lambda(T)\left(\frac{dT}{dx}\right)_{x=0} = \rho c \Delta x \frac{dT}{dt}$$

The first term describes the absorbed solar heat flux, with A=0.03 being the bolometric Bond albedo of the surface, S the solar constant, AU the heliocentric distance of 67P (in astronomical units), and $f_{illum}(0;1)$ a marker if the surface is shadowed. The parameter θ describes the angle between the surface normal and the solar vector. The second term $F_{scatter}$ denotes scattered light from other facets; as we assume lambertian scattering, it is a function of the nucleus geometry. Both terms are calculated using a Monte Carlo ray-tracing method.

Cliff wall and plateau facet temperatures are given by T_i, facets that create the radiative environment for every facet i are denoted by j≠i, their temperature is T_j. Infrared radiative exchange is accounted for in the third term: REF is the radiative exchange factor between surfaces in contact; for facets whose area is small compared to its distance r_{ij}^2 it can be approximated by

$$REF_{i,j} = dA_j\varepsilon^2\sigma\ \frac{\cos\delta_i\cos\delta_j}{\pi r_{ij}^2}$$

Here, δ specifies the angle between the facet normal to the connection vector between both surfaces i and j; the emissivity ε is assumed to be 0.97, and the Stefan-Boltzmann-Constant is denoted by σ. $REF_{i,j}$ values are calculated using a Monte Carlo ray-tracing method, this method includes scattering at other facets.

The fourth term describes the thermal infrared emission to other surface element and to space. We neglect thermal emission and backscattering of the dust coma.

The fifth term is the conductive heat flux, dependent on conductivity $\lambda(T)$ and temperature gradient $\frac{dT}{dx}$ between the surface node und the neighboring node underneath, as described in Equation 1.

The term on the right side of the equation describes the nodal energy storage and consists of density ρ (being 530 kg/m³, within the range of values determined by [40]), the nodal height Δx, and the material heat capacity c (assumed 800 J/kgK). We deviate from the widely accepted approach of formulating a surface boundary that is in instantaneous radiative equilibrium with the environment. As our model assumes a highly porous cometary material composed of agglomerates of grains, solar irradiation penetrates to small depths until being fully absorbed. Any instant equilibrium leads to unphysical, extremely high gradients at the onset of solar illumination. As this analysis focuses on the estimation of thermal gradients in the subsurface layers, the usage of a boundary node with non-zero thermal capacity circumvents this problem without neglecting the basics of heat transfer.

At a depth of 5 cm, diurnal temperature variations are less than one degree. Hence, we are safe to assume an adiabatic boundary condition at a depth of 0.35 m.

$$\left(\frac{dT}{dx}\right)_{x=0.35m} = 0$$

The SHAP4S digital terrain model of 67P is scaled down to roughly 100k triangular facets. Each of these facets represents a single surface node of the geometrical model. This resolution allows for a compromise between high accuracy of the modelled terrain and its implications on shadowing and self-heating, while significantly reducing the computational time required for the analysis. A typical facet has side lengths of about 10 meters, so 3D heat transfer within the cometary layers can be neglected [41]. We apply two thermal environments: for the 10 May 2015, we use a tilt of the comet rotation axis of 0.2 degrees and a heliocentric distance of 1.76 AU; the 10 July 2015 applies 30.3 degrees and 1.31 AU [28]. We tested other dates in order to verify the tendency of the presented results. We calculate the solar irradiation pattern for every 5 degrees of an entire comet rotation, which results in one position every 10 minutes and a total of 72 calculated patterns. Between these positions, we interpolate linearly to obtain the time-dependent solar irradiation function for every facet. The temperature distribution in the surface layers of the cliff area is modelled with 20 nodal layers, each between 1mm and 70 mm in depth.

In contrast, the nodes that form the radiative environment (all nodes that are not part of the cliff itself) are modelled in a more simple way. These nodal temperatures are calculated by the following approach that neglects subsurface conduction:

$$(1 - A)\frac{S}{AU^2} f_{illum} \cos\theta + F_{scatter} + \sum_j REF_{i,j} T_j^4 - \varepsilon\sigma T_i^4 = \rho c \Delta x \frac{dT}{dt}$$

We calculate temperatures for a time step of one minute with a Crank Nicholson numerical scheme (e.g. [42]). After 40 rotational periods, the results converged to temperature deviations of less than 0.1 K. Supplementary Figure 3 is an example that shows the surface temperatures for 67P for two moments, separated by twenty minutes and showing the sharp temperature increase over short period of time at the Aswan cliff wall.

Boulder Analysis Methodology:

The identification of the boulders located on the Aswan talus, both pre- and post-collapse, was performed with the ArcGis software. We made use of three NAC images (Supplementary Table 1) that were obtained at distances ranging between 25.4 and 29.5 km from the cometary surface and a corresponding scale of 0.48-0.55 m/px. By considering the minimum three-pixels sampling rule, that minimizes the likelihood of misidentifications of what we are detecting [43], we set the lowest measurable boulder size at 1.5 m. The constant presence of shadows next to the boulders (the observations were performed with phase angles varying from 47° to 77°), allowed us to identify even smaller boulders (2 pixels diameter, ~1 m). However, as indicated in [20], we did not include these smaller populations in the cumulative size-frequency distribution (SFD) because they do not represent a complete dataset for such small sizes, as demonstrated by the clear roll-over below 1.5 m. Like [44-46], we considered a "boulder" (we underline that this terminology is not meant to imply any structural similarity to the boulders normally seen on Earth, but when we identified a feature with the mentioned characteristics, we inferred that it was a boulder) to be a positive relief detectable in various images obtained with different observation geometries, with a constant elongated shadow (if the phase angle is greater than 0°). Furthermore, the boulder needs to appear detached from the ground on which it stands.

After these features were visually identified in the images, we measured their positions on the surface of the comet and assumed their shapes to be circumcircles. Then, we derived their diameters and the corresponding areas (see Supplementary Figure 4). Consequently, in order to obtain the cumulative boulder size-frequency distribution (SFD) per km^2, we divided the cumulative numbers by the corresponding total terrace area, 0.056 km^2, computed from the 3D shape model of 67P [11]. In the log-log plot, we then fitted a regression line to the binned data to obtain the power-law index of each size distribution, while the error bars for each value indicate the root of the cumulative number of counting boulders following [47]. We finally underline that the regression line does not take into account those points that are cumulatively repeated, i.e. above 6.5 m. Indeed this is an indication of a poor statistics, and if considered by the fit, it could lead to biased power-law indices.

The power-law index of the boulder size-frequency distribution (SFD) carries information about the boulder formation and evolution processes occurring both on comets, asteroids and on planetary bodies [20,48,49,50]. The resulting power-law index we obtained for the Aswan pre-collapse case is -3.27 +0.21/-0.22 (Supplementary Figure 5), indicative of a mixture of two boulder populations: the talus population is located at the base of the cliff where thermal fracturing and consequent sublimation occurs [20] and is characterised by a higher density of smaller (< 4 m) boulders; while the distal detrital deposit [22] is located further out from the cliff and shows larger blocks with sizes > 5 m and likely originated from an initial ceiling collapse forming the whole plateau [20,22]. The resulting pre-collapse cumulative number of boulders per $km^2 \geq 1.5$ m is 11784. After the collapse, a new talus appeared below the wall resulting in a steeper power-law index of -3.61 +0.20/-0.31 and a cumulative number of boulders per $km^2 \geq 1.5$ m of 18438. When comparing the two SFDs (Supplementary Figure 5 and Supplementary Table 2) the main post-collapse difference is in the number increase of the bin sizes between 1.5 and 3.0 m that causes the steepening of the power-law index. The clear blanketing effect of the boulders ≤ 3 m is observable in Supplementary Figure 6. We point out that the -3.61 +0.20/-0.31 power-law index is consistent with the predicted range of -3.5 to -4.5, suggested by [20] to be related to gravitational events triggered by sublimation and/or thermal fracturing and supports the interpretation of a fresh gravitational accumulation for this deposit. In addition, the boulder distribution that we derive in the Aswan talus highlights the fact

that the collapsing block has produced predominantly smaller chunks, as detailed in the Main Text.

In order to quantify the sensitivity of the presented results to the detected boulders, we performed a numerical experiment in which we randomly changed the diameter of such boulders, within selected ranges. Such analysis was performed both for the pre- and post-collapse cases (Supplementary Figure 5). In particular, each previously detected diameter was first independently perturbed by randomly adding an error sampled through a Monte Carlo procedure from uniform distributions in the ranges from ±0.005 to ±1.0 m, secondly the SDF and the power-law index was recomputed in the same range of diameters previously adopted, i.e. from 1.5 to 6.5 m. We note that an error of ±1.0 m means an over- or underestimation of 2 pixels, which is highly unlikely given that all the considered boulders were detected above the three pixel sampling rule [44]. On the contrary, an over or underestimation smaller than half pixel, i.e. ±0.25, is more plausible given that we are considering only those boulders with dimensions above the three pixel sampling threshold. For each selected perturbation we performed 10^5 simulations. The results are presented in Supplementary Figure 7. As expected, in the case of minimal size changes, the obtained median values coincide with the power-law indices previously computed, i.e. -3.21 and -3.61 for the pre- and post-collapse case, respectively. On the contrary, when increasing the diameter perturbations the analysis shows a decrease of the median values of the power-law index in the pre-collapse study, up to 1.6% for the ±1.0 m case, (i.e. from -3.21 to -3.27), while it shows an increase in the post-collapse scenario, up to 2.95% in the same ±1.0 m range (i.e. from -3.61 to -3.72). In addition, both the pre- and post-collapse cases show a comparable increased variability in the power-law indices with an increasing range of the selected perturbations. Nonetheless, even when bigger perturbations are taken into account (1-2 pixels), the analysis suggest well distinct power-law indices, corroborating our hypothesis of a lower power-law index for the pre-collapse case with respect to the post-collapse one.

Data Availability Statement

All data presented in this paper will be delivered to ESA's Planetary Science Archive (http://www.rssd.esa.int/index.php?project5PSA&page5rosetta) and NASA's Planetary Data System (https://pds.nasa.gov/) in accordance with the schedule established by the Rosetta project. The authors declare no competing financial interests. Readers are welcome to comment on the online version of the paper.

Methods References

30) Hapke, B. Bidirectional Reflectance Spectroscopy. 5. The Coherent Backscatter Opposition Effect and Anisotropic Scattering. *Icarus* **157**, 523-534 (2002).

31) Hapke, B. The opposition effect of the moon - The contribution of coherent backscatter. *Science* **260**, 509-511 (1993).

32) Anderson, J. A. *et al.* Modernization of the Integrated Software for Imagers and Spectrometers in Lun. Planet. Sci. Conf., eds. S. Mackwell, & E. Stansbery, *Lunar and Planetary Inst. Technical Report*, **35**, 2039 (2004).

33) Oklay, N. *et al.* Variegation of comet 67P/Churyumov-Gerasimenko in regions showing activity. *Astron. Astrophys.* **586**, A80, 18 pp (2016).

34) Weissmann, P.R. and Kieffer, H. H. An improved thermal model for cometary nuclei. *J. Geophys. Res.* **89**, p. C358-C364 (1984).

35) Spencer, J. R. A rough-surface thermophysical model for airless planets. *Icarus* **83**, 27–38 (1990).

36) Rozitis, B. & Green, S. F. Directional characteristics of thermal-infrared beaming from atmosphereless planetary surfaces - a new thermophysical model. *Mon. Not. R. Astron. Soc.* **415**, 2042–2062 (2011).

37) Gundlach, B. and Blum, J. Outgassing of icy bodies in the Solar System – II: Heat transport in dry, porous surface dust layers. *Icarus* **219**, 618-629.

38) Schloerb, F. P. *et al.* MIRO observations of subsurface temperatures of the nucleus of 67P/Churyumov-Gerasimenko. *Astron. Astrophys.* **583**, A29, 11 pp (2015).

39) Lowry, S. *et al.* The nucleus of Comet 67P/Churyumov-Gerasimenko. A new shape model and thermophysical analysis. *Astron. Astrophys.* **548**, A12, 15 pp (2012).

40) Jorda, L. *et al.* The global shape, density and rotation of Comet 67P/Churyumov-Gerasimenko from preperihelion Rosetta/OSIRIS observations. *Icarus* **277**, 257-278 (2016).

41) Davidsson, B.J.R. and Rickman, H. Surface roughness and three-dimensional heat conduction in the thermophysical models. Icarus **243**, 58-77.

42) Tan L. Efficient algorithms for Crank-Nicholson-based-finite-difference time-domain methods. *IEEE Transactions on microwave theory and techniques*, **56**, no. 2 (2008).

43) Nyquist, H. Certain topics in telegraph transmission theory. *Trans. Am. Inst. Elect. Eng.*, **47**, 617 (1928).

44) Pajola, M. *et al.* Size-frequency distribution of boulders ≥10 m on comet 103P/Hartley 2. *Astron. Astrophys.* **585**, A85, 8 pp (2016).

45) Pajola, M. *et al.* The southern hemisphere of 67P/Churyumov-Gerasimenko: Analysis of the preperihelion size-frequency distribution of boulders ≥7 m. *Astron. Astrophys.* **592**, id.L2, 5 pp (2016).

46) Pajola, M. *et al.* The Agilkia boulders/pebbles size-frequency distributions: OSIRIS and ROLIS joint observations of 67P surface. *Mon. Not. R. Astron. Soc.* **462**, 242–252 (2016).

47) Michikami, T. *et al.* Size-frequency statistics of boulders on global surface of asteroid 25143 Itokawa. *Earth, Planets and Space*, **60**, 13-20 (2008).

48) Thomas, P. *et al.* Shoemaker crater as the source of most ejecta blocks on the asteroid 433 Eros. *Nature*, **413**, 394-396 (2001).

49) Bart, G. D. and Melosh, H. J. Distributions of boulders ejected from lunar craters. *Icarus*, **209**, 337-357 (2005).

50) Golombek, M., and Rapp D. Size-frequency distributions of rocks on Mars and Earth analog sites: Implications for future landed missions. *J. Geophys. Res.* **102**, 4117- 4129 (1997).
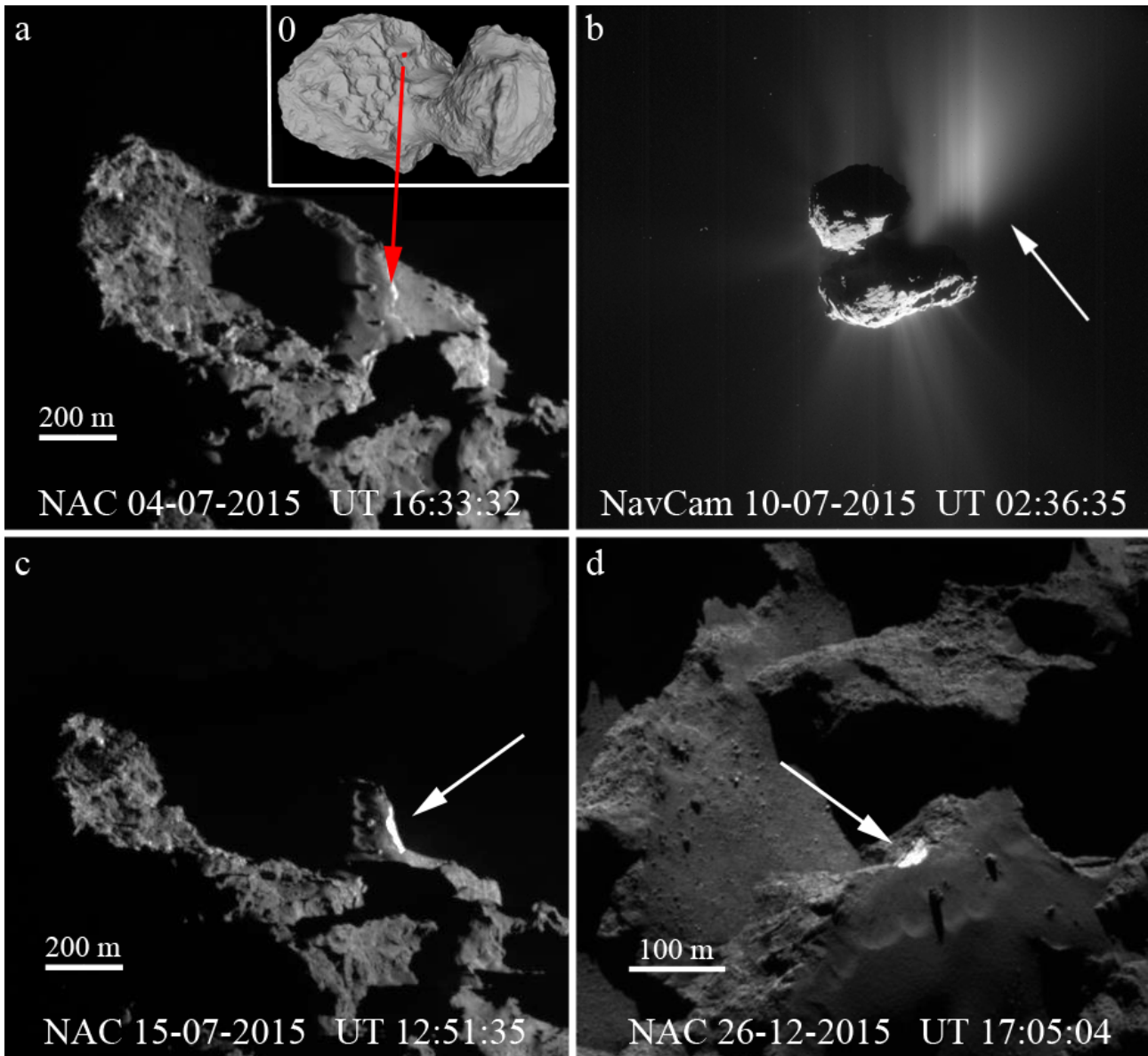
Figure 1.

917x847 pixels

PNG version 554 Kb

EPS version 6.4 Mb

PSD version 3.7 Mb

Figure 2.

2834x2854 pixels

PNG version 5.9 Mb

EPS version 65.9 Mb

PSD version 39.7 Mb
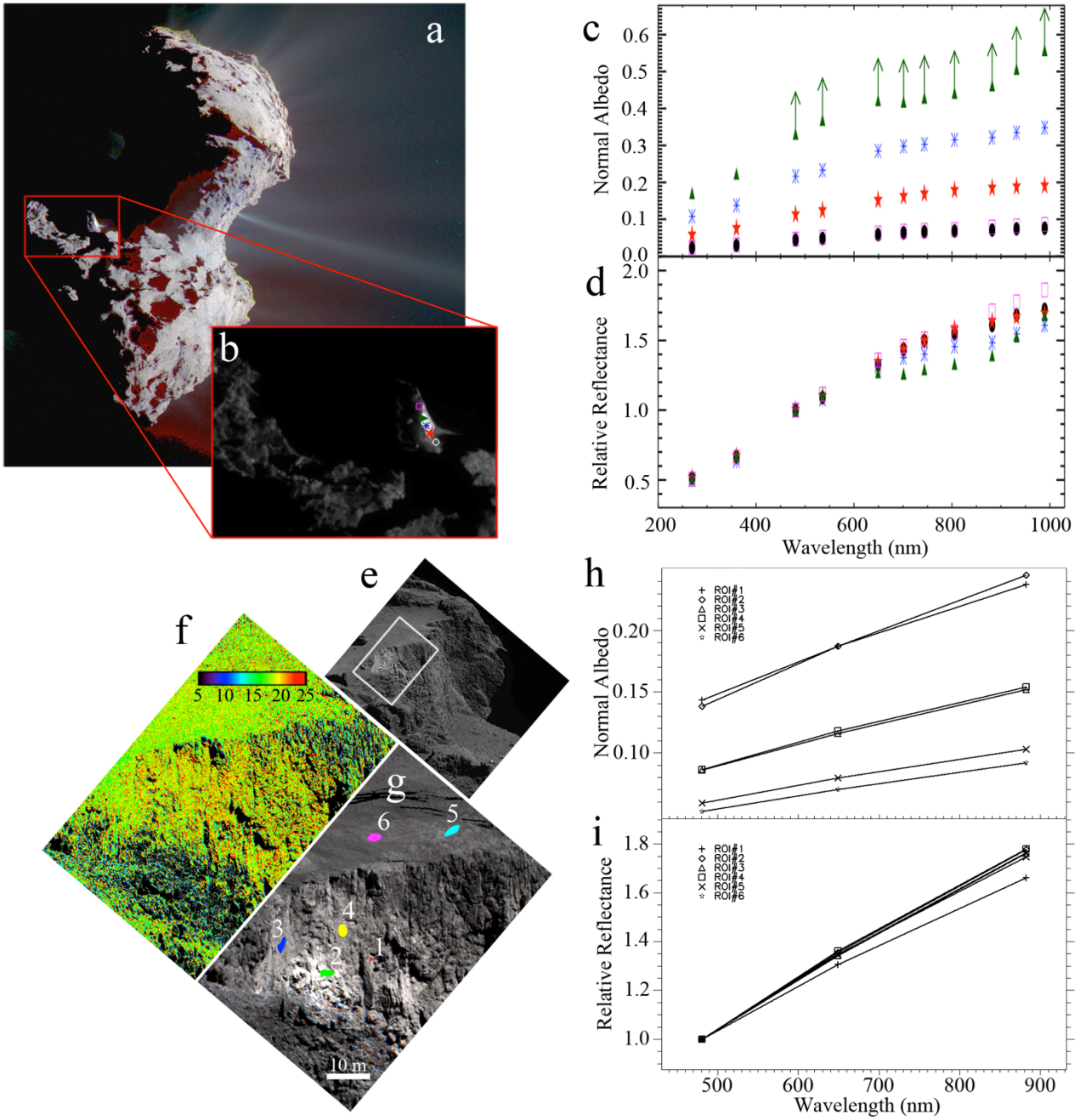
Figure 3.

2088x2152 pixels

PNG version 2.5 Mb

EPS version 36.7 Mb

PSD version 9.8 Mb

Figure 4.

2121x2499 pixels
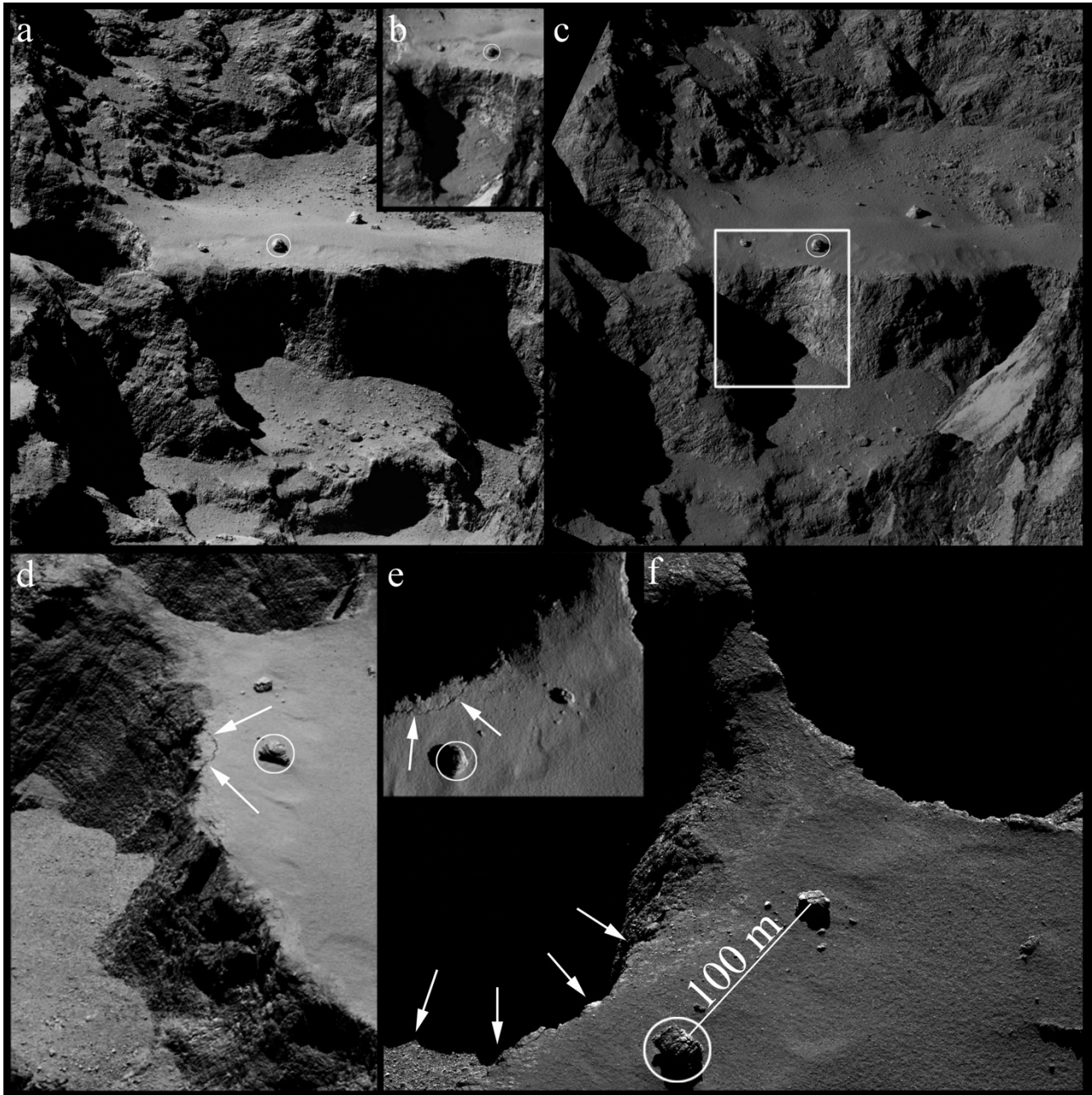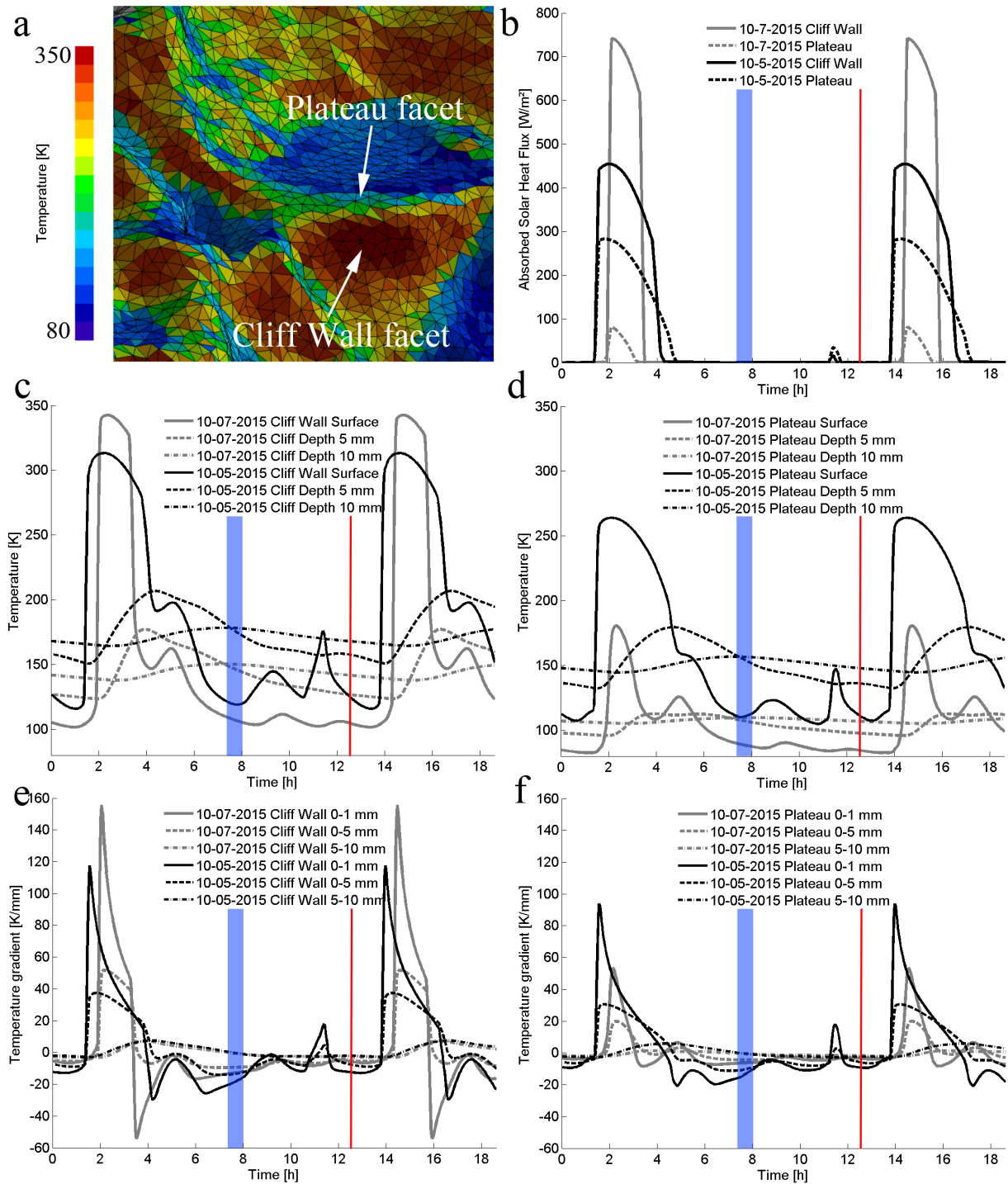
PNG version 986 Kb

EPS version 43.2 Mb

PSD version 5.9 Mb
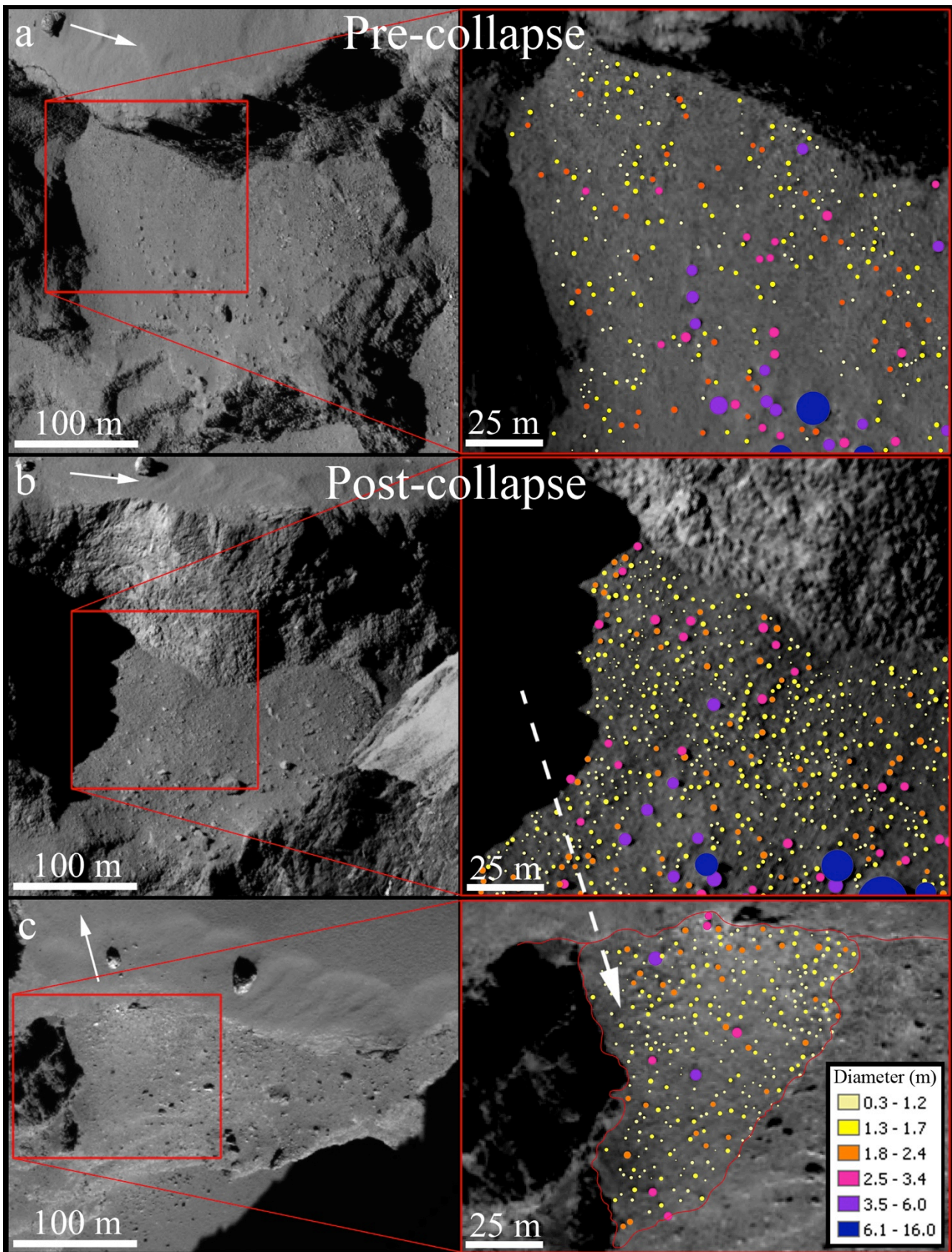
Figure 5.

1739x2294 pixels

PNG version 3.0 Mb

EPS version 32.6 Mb

PSD version 25.3 Mb

The pristine interior of comet 67P revealed by the combined Aswan outburst and cliff collapse

M. Pajola et al.

Supplementary Material

Figures
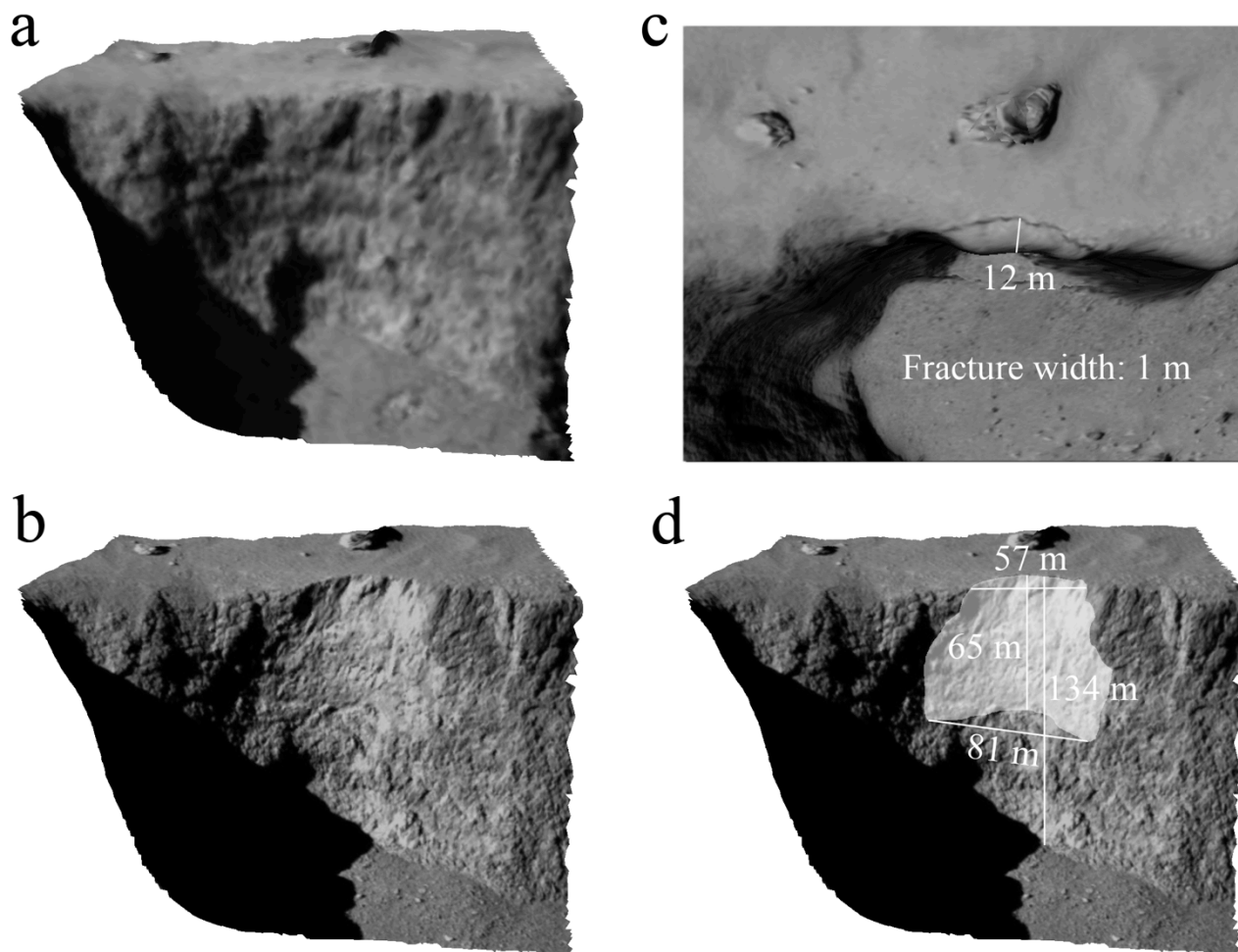
Supplementary Figure 1. a, 3D view of the Aswan cliff before the collapse (see Fig. 2c for context). **b,** 3D view of the cliff after the breakdown. **c,** 3D view showing the maximum distance between the pre-collapse overhang and the new cliff edge. The fracture width is also indicated. **d,** dimensions of the detached wall computed on the 67P shape model.
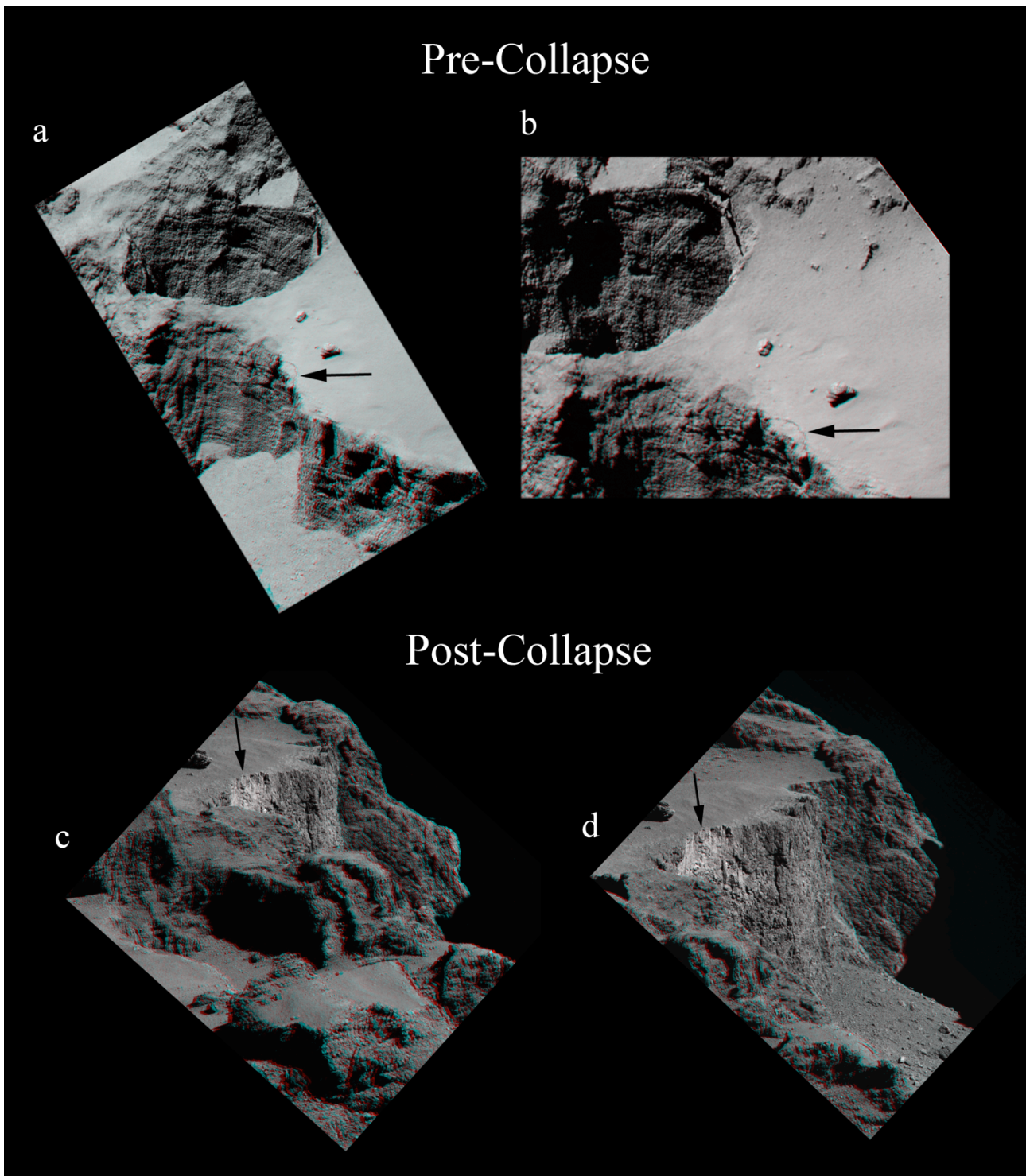
Supplementary Figure 2. Four different anaglyph views prepared for evaluating the considered volume of the overhang that detached in July 2015. The black arrows show the location of the fracture before the collapse, and the edge of the new cliff after the breakdown.
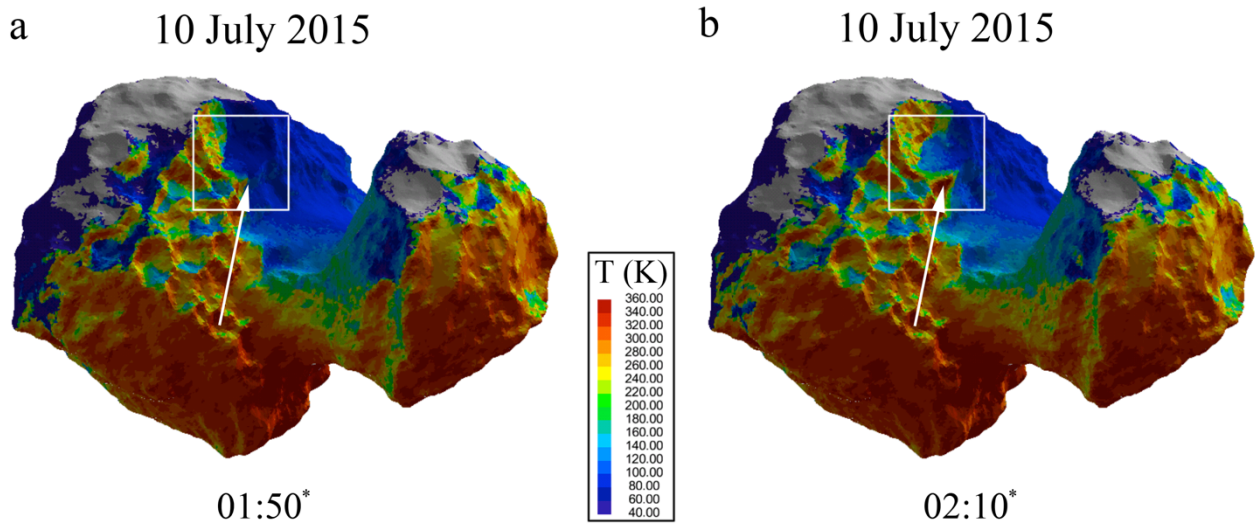
Supplementary Figure 3. a, Surface temperature on 67P obtained after 1:50 h from the beginning of one diurnal period of 67P (* is simulation time, not UT time). **b,** Surface temperature on 67P obtained 20 min after the **a** case. The white square is the Aswan area of Fig. 4a. The white arrows show the location of the breakdown. Grey areas show temperatures < 40 K.
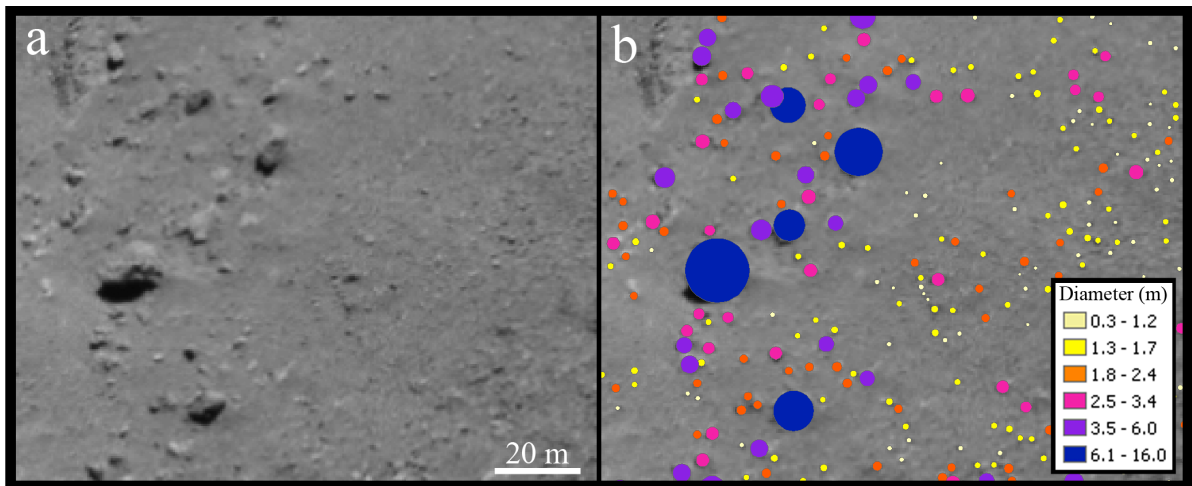
Supplementary Figure 4. Example of the methodology used to identify the boulders on the Aswan talus. **a,** Subframe of an OSIRIS NAC image with a scale of 0.48 m/px. **b,** The same image with the detected boulders grouped by size (m).
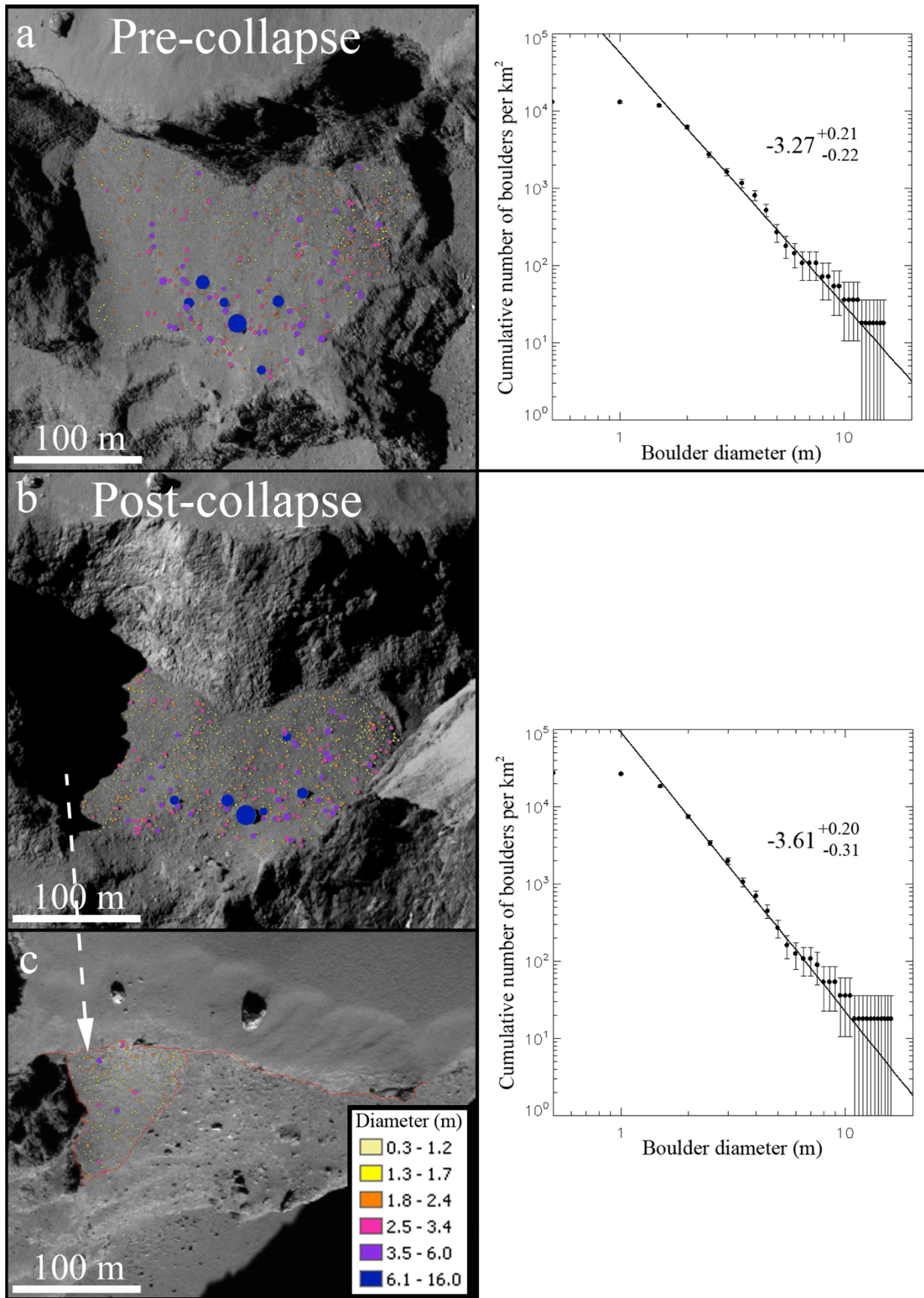
Supplementary Figure 5. First column: the three NAC images overlaid with the spatial distribution of the boulders grouped in size (m). Second column: the SFD of the boulders computed for the pre- and the post-collapse (both computed in the 1.5-6.5 m range, see Supplementary Table 2), together with the corresponding power-law index.
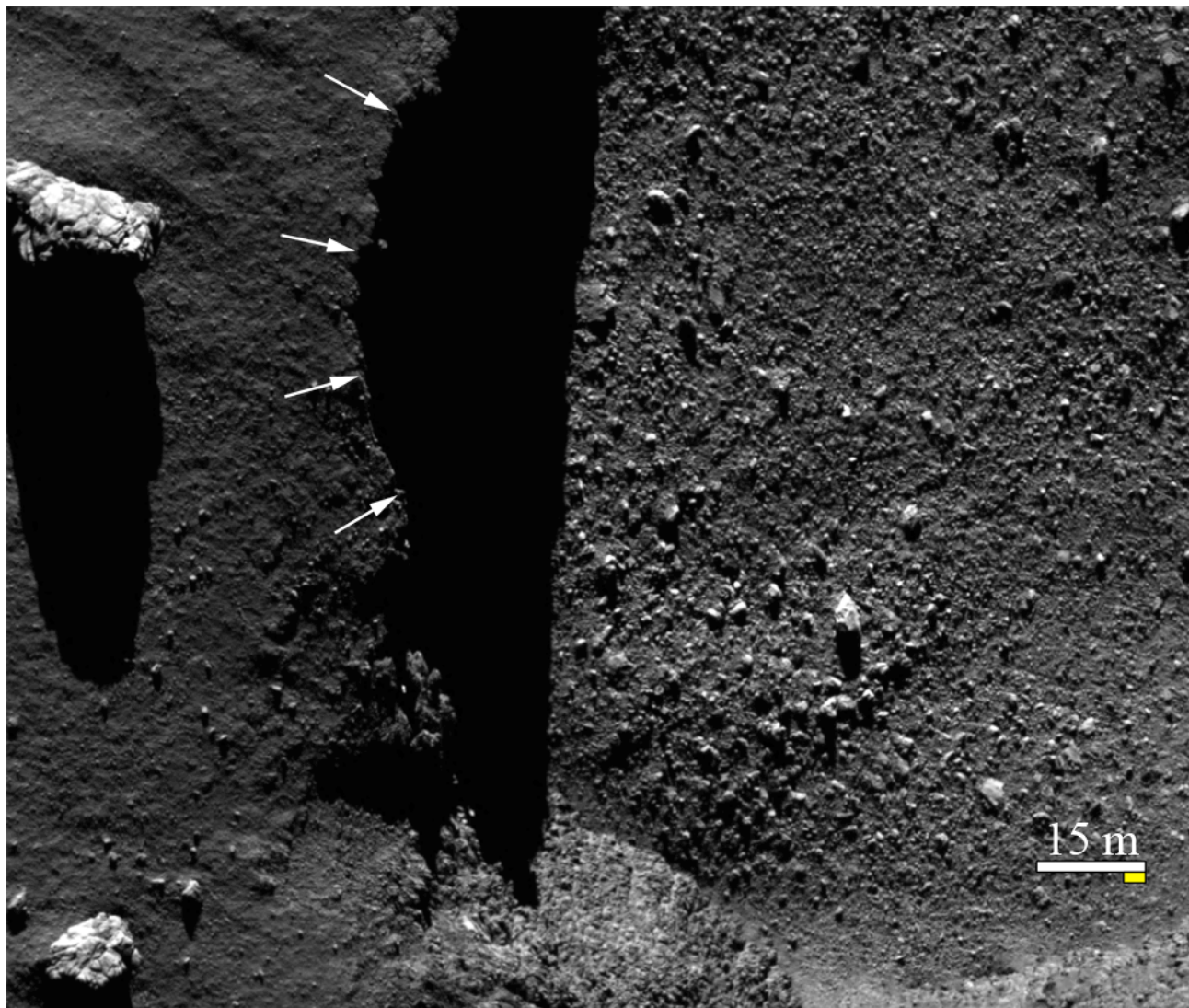
Supplementary Figure 6. OSIRIS NAC image obtained on 6 August 2016 at 16:56:48 UT from a distance of 7.80 km from the surface and a corresponding scale factor of 0.14 m/pixel. The white bar is 15 m long, while the yellow one is 3 m. It is evident how the typical sizes of the chunks below the cliff are below 3-3.5 m. The white arrows mark the limit of the collapsed cliff.
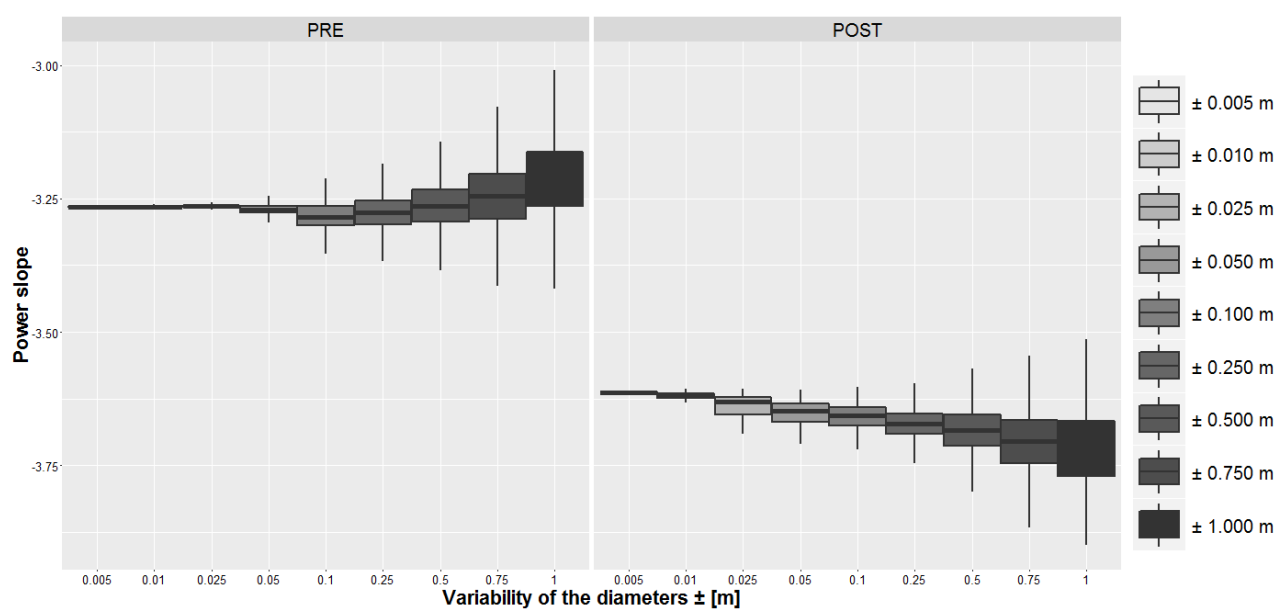
Supplementary Figure 7. Sensitivity analysis - box plots of the power-law indices obtained by varying the size of the identified boulders by different values, i.e. from ±0.005 to ±1.000 m. The upper and lower hinges correspond to the 25th and 75th percentiles; the whiskers extend from the minimum to the maximum values.

Tables

Figure (Panel)	Instrument	Acquisition time (year-month-dayThh.mm.ss) in UTC	Rosetta-Sun distance (AU)	Phase Angle (°)	Filter	Wavelength (nm)	Rosetta - 67P center distance (km)	Spatial Scale (m/pixel)
1a	OSINAC	2015-07-04T16.33.32	1.33	89.70	F23	535.7	173.84	3.24
1b	NavCam	2015-07-10T02.36.35	1.31	90.04	/	/	156.58	15.81
1c	OSINAC	2015-07-15T12.51.35	1.29	89.55	F22	649.2	164.51	3.06
1d	OSINAC	2015-12-26T17.05.04	1.97	89.44	F22	649.2	77.05	1.41
2a	OSINAC	2014-09-19T13.42.48	3.33	68.82	F22	649.2	28.29	0.50
2b	OSINAC	2015-03-20T01.17.47	2.05	50.99	F22	649.2	80.72	1.48
2c	OSINAC	2016-06-08T14.34.26	3.16	46.82	F22	649.2	29.72	0.52
2d	OSINAC	2014-09-21T01.09.01	3.32	62.32	F22	649.2	27.61	0.48
2e	OSINAC	2014-09-22T04.44.19	3.31	67.85	F22	649.2	28.14	0.49
2f	OSINAC	2016-05-18T23.53.37	3.03	89.60	F22	649.2	8.40	0.12
3a-d	OSINAC	2015-07-19T04.06.41	1.28	89.13	F23	535.7	179.87	3.35
3a-d	OSINAC	2015-07-19T04.06.52	1.28	89.13	F22	649.2	179.87	3.35
3a-d	OSINAC	2015-07-19T04.07.04	1.28	89.13	F41	882.1	179.87	3.35
3a-d	OSINAC	2015-07-19T04.07.16	1.28	89.13	F24	480.7	179.87	3.35
3a-d	OSINAC	2015-07-19T04.07.27	1.28	89.13	F71	989.3	179.86	3.35
3a-d	OSINAC	2015-07-19T04.07.42	1.28	89.13	F27	701.2	179.86	3.35
3a-d	OSINAC	2015-07-19T04.07.54	1.28	89.13	F51	805.3	179.86	3.35
3a-d	OSINAC	2015-07-19T04.08.05	1.28	89.13	F61	931.9	179.86	3.35
3a-d	OSINAC	2015-07-19T04.08.18	1.28	89.13	F28	743.7	179.85	3.35
3a-d	OSINAC	2015-07-19T04.08.29	1.28	89.13	F16	360.0	179.85	3.35
3a-d	OSINAC	2015-07-19T04.08.42	1.28	89.13	F15	269.3	179.85	3.35
3e-i	OSINAC	2016-08-06T07.08.36	3.52	72.39	F24	480.7	8.35	0.12
3e-i	OSINAC	2016-08-06T07.08.48	3.52	73.39	F22	649.2	8.35	0.12
3e-i	OSINAC	2016-08-06T07.08.59	3.52	74.39	F41	882.1	8.35	0.12
5a	OSINAC	2014-09-21T02.34.51	3.32	62.37	F41	882.1	27.59	0.48
5b	OSINAC	2016-06-08T14.34.26	3.16	46.82	F22	649.2	29.72	0.52
5c	OSINAC	2016-06-18T01.36.36	3.22	68.63	F22	649.2	30.85	0.54
Suppl. 2a	OSINAC	2014-09-21T01.09.01	3.32	62.32	F22	649.2	27.61	0.48
Suppl. 2a	OSINAC	2014-09-21T01.09.52	3.32	62.32	F41	882.1	27.61	0.48
Suppl. 2b	OSINAC	2014-09-21T01.42.48	3.32	62.34	F22	649.2	27.6	0.48
Suppl. 2b	OSINAC	2014-09-21T01.43.39	3.32	62.34	F41	882.1	27.6	0.48
Suppl. 2c	OSINAC	2016-08-06T07.08.36	3.52	72.39	F24	480.7	8.35	0.12
Suppl. 2c	OSINAC	2016-08-06T07.08.59	3.52	72.38	F41	882.1	8.35	0.12
Suppl. 2d	OSINAC	2016-08-06T07.23.36	3.52	72.15	F24	480.7	8.35	0.12
Suppl. 2d	OSINAC	2016-08-06T07.23.59	3.52	72.14	F41	882.1	8.35	0.12
Suppl. 4	OSINAC	2014-09-21T02.34.51	3.52	62.37	F41	882.1	27.59	0.48
Suppl. 5a	OSINAC	2014-09-21T02.34.51	3.32	62.37	F41	882.1	27.59	0.48
Suppl. 5b	OSINAC	2016-06-08T14.34.26	3.16	46.82	F22	649.2	29.72	0.52
Suppl. 5c	OSINAC	2016-06-18T01.36.36	3.22	68.63	F22	649.2	30.85	0.54
Suppl. 6	OSINAC	2016-08-06T16.56.48	3.52	77.54	F22	649.2	9.34	0.14

Supplementary Table 1. List of all images used in this work. OSINAC refers to the OSIRIS Narrow Angle Camera images, while NavCam refers to the Rosetta Navigation Camera image.

Pre

Bin	Frequency	Cumulative no.	Error cumul. no.	Cumulative no. sq. km	Error cumulative no. sq km
1.5	312	657	25.63	11784	459.73
2.0	193	345	18.57	6188	333.14
2.5	61	152	12.33	2726	221.13
3.0	26	91	9.54	1632	171.09
3.5	20	65	8.06	1166	144.60
4.0	16	45	6.71	807	120.32
4.5	14	29	5.39	520	96.59
5.0	5	15	3.87	269	69.46
5.5	2	10	3.16	179	56.72
6.0	2	8	2.83	143	50.73
6.5	0	6	2.45	108	43.93
7.0	0	6	2.45	108	43.93
7.5	2	6	2.45	108	43.93
8.0	0	4	2.00	72	35.87
8.5	1	4	2.00	72	35.87
9.0	0	3	1.73	54	31.07
9.5	1	3	1.73	54	31.07
10.0	0	2	1.41	36	25.36
10.5	1	2	1.41	36	25.36
11.0	0	1	1.00	18	17.94
11.5	0	1	1.00	18	17.94
12.0	0	1	1.00	18	17.94
12.5	0	1	1.00	18	17.94
13.0	0	1	1.00	18	17.94
13.5	0	1	1.00	18	17.94
14.0	0	1	1.00	18	17.94
14.5	0	1	1.00	18	17.94
15.0	0	1	1.00	18	17.94
15.5	0	1	1.00	18	17.94
16.0	1	1	1.00	18	17.94

Post

Bin	Frequency	Cumulative no.	Error cumul. no.	Cumulative no. sq. km	Error cumulative no. sq km
1.5	613	1028	32.06	18438	575.06
2.0	226	415	20.37	7443	365.38
2.5	78	189	13.75	3390	246.57
3.0	52	111	10.54	1991	188.96
3.5	20	59	7.68	1058	137.77
4.0	14	39	6.24	699	112.01
4.5	10	25	5.00	448	89.68
5.0	6	15	3.87	269	69.46
5.5	2	9	3.00	161	53.81
6.0	1	7	2.65	126	47.45
6.5	0	6	2.45	108	43.93
7.0	1	6	2.45	108	43.93
7.5	2	5	2.24	90	40.11
8.0	0	3	1.73	54	31.07
8.5	0	3	1.73	54	31.07
9.0	1	3	1.73	54	31.07
9.5	0	2	1.41	36	25.36
10.0	0	2	1.41	36	25.36
10.5	1	2	1.41	36	25.36
11.0	0	1	1.00	18	17.94
11.5	0	1	1.00	18	17.94
12.0	0	1	1.00	18	17.94
12.5	0	1	1.00	18	17.94
13.0	0	1	1.00	18	17.94
13.5	0	1	1.00	18	17.94
14.0	0	1	1.00	18	17.94
14.5	0	1	1.00	18	17.94
15.0	0	1	1.00	18	17.94
15.5	0	1	1.00	18	17.94
16.0	1	1	1.00	18	17.94

Supplementary Table 2. The frequency and cumulative numbers, both absolute and per km^2 of the pre- and post-collapse boulder analysis. The yellow raw indicates the size limit used to compute the power-slope indices.

Videos

Supplementary Video 1. Video representation of the illumination conditions at the Aswan cliff and plateau on 10 July 2015.